PAPER • OPEN ACCESS

Optimizing dynamic measurement accuracy for machine tools and industrial robots with unscented Kalman filter and particle swarm optimization methods

To cite this article: Kanglin Xing *et al* 2024 *Meas. Sci. Technol.* **35** 085601

OPEN ACCESS
IOP Publishing
Measurement Science and Technology
Meas. Sci. Technol. **35** (2024) 085601 (20pp)
https://doi.org/10.1088/1361-6501/ad4666

Optimizing dynamic measurement accuracy for machine tools and industrial robots with unscented Kalman filter and particle swarm optimization methods

Kanglin Xing[1], Ilian A Bonev[2], Henri Champliaud[1] and Zhaoheng Liu[1,*]

[1] Department of Mechanical Engineering, École de technologie supérieure, 1100 Notre-Dame St W, Montreal, Quebec H3C 1K3, Canada
[2] Department of Systems Engineering, École de technologie supérieure, 1100 Notre-Dame St W, Montreal, Quebec H3C 1K3, Canada

E-mail: zhaoheng.liu@etsmtl.ca

Received 26 January 2024, revised 2 April 2024
Accepted for publication 2 May 2024
Published 13 May 2024

Abstract

The telescoping ballbar is widely utilized for diagnosing accuracy and identifying faults in machine tools and industrial robots. Currently, there are no established standards for determining the optimal feed rate for ballbar tests. This lack of clear guidelines results in time inefficiency in measurements and inconsistencies in dynamic measurements, which complicates the comparison of ballbar test results under various conditions or across different machine platforms. To mitigate dynamic variations in ballbar results, an updated ballbar data processing method that integrates the unscented Kalman filter (UKF) and particle swarm optimization (PSO) was developed and validated using real ballbar data measured at multiple feed rates and simulated data with varying vibration magnitudes generated through the Renishaw ballbar simulator. Experimental results revealed that the dynamic components extracted from the ballbar results were observed to increase in correlation with the vibration measured at different feed rates and from the simulations. Moreover, the variations in the results measured at different feed rates after PSO-UKF processing were significantly reduced. The findings confirm the effectiveness of the proposed method in minimizing the dynamics of the ballbar results. Ultimately, this approach enhances the efficiency and accuracy of ballbar testing and offers a general method for improved diagnostics.

Keywords: dynamic components, telescoping ballbar, unscented Kalman filter (UKF), particle swarm optimization (PSO)

* Author to whom any correspondence should be addressed.

Nomenclature

UKF	unscented Kalman filter
PSO	particle swarm optimization
GD	gradient descent
GA	genetic algorithms
DC	dynamic component
DTW	dynamic time warping
CD	circular deviation
HMC	hexapod machining cell
CCW	counter-clockwise
CW	clockwise
RMS	root mean square

1. Introduction

As a fundamental component in the contemporary manufacturing industry, computer numerical control (CNC) machine tools are extensively utilized to produce high-quality parts encompassing diverse materials, shapes, and dimensional tolerances. In recent years, significant attention has been focused on accuracy assessment and error compensation of machine tool errors, aiming for a deeper understanding and enhancement of machine tool accuracy [1]. Geometric error measurement commonly employs tools such as laser interferometer systems, laser trackers, ballbars, R-tests, and a combination of 2D artifacts and 3D ball plates with touch-trigger probes [2]. The choice of error measurement method depends on the geometry of the machine tool and specific measurement objectives. However, the ballbar is unparalleled in terms of minimizing measurement time and simplifying the measurement procedure.

The telescoping ballbar, first proposed and patented by Bryan in 1982 [3], revolutionized the measurement of radial changes in circular motion using an accurate linear scale sensor. Since their introduction, ballbars have been extensively applied in circular tests [4, 5], calibration of rotary axes [6, 7], assessment of the thermal or geometrical behavior of five-axis machine tools [8, 9], kinematic calibration of parallel kinematic machines [10], and industrial robots [11]. As an efficient automated tool conforming to ISO 230-4 standards, the telescoping ballbar excels in error detection in machine tools and industrial robots, ensuring precise error identification [12]. It evaluates the accuracy of circular contouring by monitoring machine axis movements along a predetermined circular trajectory, and presents results in a polar format for easy interpretation [13]. When integrated with commercial ballbar analysis software, such as Renishaw Ballbar 20, this tool can identify various error sources, such as backlash, scale mismatch, and squareness, thereby enhancing its utility and reliability. This comprehensive analysis aids in improving the positioning performance of machine tools. The velocity of a machine impacts its dynamics, particularly at different feed rates, influencing the vibrations detected in a ballbar test. At lower speeds, the dynamic load is minimal owing to the machine's high stiffness, resulting in negligible vibrations but potentially longer measurement times, particularly with larger ballbar radii [14]. Conversely, higher feed rates reduce the testing time but may introduce significant vibrations that affect ballbar accuracy. Renishaw suggested guidelines for selecting feed rates, whereas the B5.54 standard [15] recommends using 10% and 80% of the machine's maximum feed rate for ballbar tests. Higher feed rates are advantageous for detecting servo-dynamic errors, such as following errors, servo mismatch errors, and reversal spikes, as they facilitate quicker axis velocity changes. These rates are also effective for assessing the capability of a machine to rapidly interpolate small circular features. On the other hand, lower feed rates diminish servo-dynamic errors, providing a clearer insight into geometric errors, such as squareness, scaling, and straightness. Considerable flexibility remains in choosing lower speed ranges, although DCs persist in ballbar results, which current commercial ballbar software tools cannot decompose. Furthermore, the magnitude of the DCs within the standard ballbar results remains unknown. To enhance the reliability of ballbar outcomes and minimize variations in the results measured at different feed rates, an updated ballbar data processing method with dynamic error decomposition is crucial for processing ballbar results.

Various methods are available to measure and decompose dynamic-related errors. One approach involves using additional hardware. For example, Liu *et al* [16] employed a stepped-feature workpiece to correlate the geometric errors of a machine tool with workpiece features. Through on-machine measurements and calibration using a coordinate measurement machine, they successfully identified seven geometric and dynamic errors. Similarly, Andolfatto *et al* [14] effectively utilized a capball-based method to decompose both quasi-static and dynamic geometric errors in multiaxis machine tools. Another strategy employs advanced algorithms, such as the Kalman filter, to estimate the dynamic errors in robots and machine tools. Notably, the kinematic parameters and vibrations of an industrial robot were efficiently estimated and reduced using the Kalman filter proposed by Elvira-Ortiz [17]. Brecher extended this approach by applying the UKF to model various machine tool errors, effectively addressing nonlinearity and noise issues [18]. Kalman-related techniques are particularly noteworthy for their good integration into data-processing workflows, obviating the need for supplementary hardware. This makes them a practical option for tackling the DCs in ballbar results. While the conventional Kalman filter is suitable for systems with linear equations, the UKF is more suitable for nonlinear real-world scenarios, demonstrating its wider applicability and effectiveness in complex environments.

PSO was originally proposed by Kennedy and Eberhart [19, 20], since then it has been used as a promising approach for optimization problems in different areas [21]. PSO is a stochastic optimization technique inspired by avian flocking behaviors [22], and is acclaimed for its straightforward implementation and adaptability in diverse applications such as parameter tuning, function optimization, and feature extraction [22]. Notable implementations of this method include the fine-tuning of covariance matrices in

the prediction of lithium-ion battery performance using the Extended Kalman Filter [23] as well as the adjustment of noise covariance matrices in ballistic target tracking with the UKF [24]. Compared with other optimization method such as the GD and GA, PSO works as a highly versatile optimization method that balances efficiency, accuracy, and rapidity across both one-dimensional and multi-dimensional problems. Its simplicity in concept and implementation, combined with the robustness against the complexity of the optimization task makes PSO extremely popular. While GA and GD have their strengths in certain scenarios, PSO's ability to adaptively navigate through diverse search spaces without the need for gradient information positions it as a preferable option, particularly when dealing with, multi-dimensional optimization problems.

To mitigate the impact of DCs on ballbar measurements, this study introduces an updated ballbar data-processing methodology that leverages the UKF and PSO. By recognizing the influence of the setup parameters on UKF's performance of the UKF, the PSO method was incorporated for optimal parameter tuning. The effectiveness of the proposed PSO-UKF method was assessed using real ballbar test data gathered at varying feed rates and simulated data with different vibration levels. Subsequently, a reliable PSO-UKF-based ballbar processing method was validated, demonstrating its applicability in shop floor environments for precise machine accuracy measurements. The proposed method not only facilitates the decomposition of DCs at varying feed rates, but also enhances the stability of the ballbar results across different speeds. The structure of the paper is as follows: sections 2 and 3 detail the ballbar measurement device and the proposed methods for decomposing the DCs, respectively. The experimental setup is outlined in section 4. An analysis of the results is presented in section 5, followed by a discussion in section 6. The paper concludes with a summary of the findings.

2. Ballbar technology for machine-tool accuracy assessment

The principles used for ballbar measurements are illustrated in figure 1, where three common setups are shown. For a given machine tool, the origin can be expressed as $P_0(X_0,\ Y_0, Z_0)$: During the ballbar measurement, this origin was established at the center of the circular interpolation. The ball attached to the spindle then undergoes circular motion with a defined radius R (figure 1). The central controlled position of the spindle is $P_1(X_1,\ Y_1, Z_1)$, and the radius (R_1) of the circular movement can be expressed as:

$$R_1 = \sqrt{(X_1 - X_0)^2 + (Y_1 - Y_0)^2 + (Y_1 - Y_0)^2} \qquad (1)$$

For an ideal machine tool, the kinematic chain has no errors, that is, $R_1 = R$. In contrast, real machine tools exhibit various errors in the kinematic chain on both the origin and spindle sides. Then, the real position of the origin and the spindle's central controlled position can be expressed as $P_0'(X_0', Y_0', Z_0')$ and $P_1'(X_1', Y_1', Z_1')$, respectively. Errors at P_0 and P_1 can be represented by the vectors $\overrightarrow{E_0} = (E_{x0},\ E_{y0}, E_{z0})$ and $\overrightarrow{E_1} = (E_{x1},\ E_{y1}, E_{z1})$, respectively. In this case, the distance between the centers of the two balls is not constant and changes with the angular position during the circular movement. Let the change in radius be ΔR (positive extension). The real radius during the ballbar measurement can be calculated by

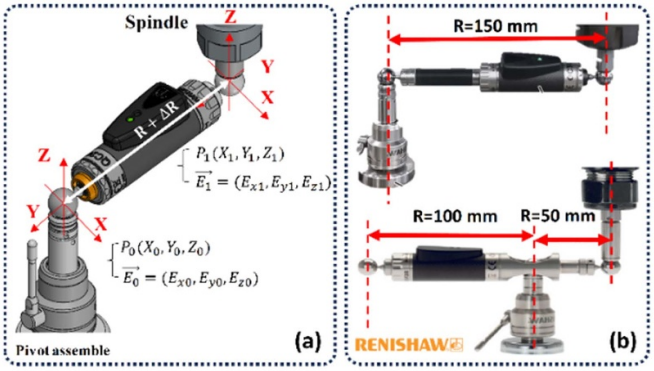

Figure 1. (a) Explanation of coordinates and error vectors in ballbar measurement, using a standard 100 mm radius setup (applicable to all ballbar sizes); (b) Overview of two different setups with different circular radii.

$$\begin{aligned} R + \Delta R &= \sqrt{(X_1' - X_0')^2 + (Y_1' - Y_0')^2 + (Z_1' - Z_0')^2} \\ &= \sqrt{\begin{array}{c}[(X_1 + E_{x1}) - (X_0 + E_{x0})]^2 + [(Y_1 + E_{y1}) - (Y_0 + E_{y0})]^2 \\ +[(Z_1 + E_{z1}) - (Z_0 + E_{z0})]^2\end{array}}. \end{aligned} \qquad (2)$$

When substituting equation (1) and ignoring the second-order terms of the errors, ΔR can be calculated as

$$\Delta R = \begin{array}{c}[(X_1 - X_0)(E_{x1} - E_{x0}) + (Y_1 - Y_0)(E_{y1} - E_{y0}) \\ +(Z_1 - Z_0)t(E_{z1} - E_{z0})]\end{array} \Big/ R. \qquad (3)$$

For simplifying the above eqs, let:

$$\begin{aligned} (X_1 - X_0, Y_1 - Y_0, Z_1 - Z_0\ ) &= (X, Y, Z) \\ (E_{x1} - E_{x0}, E_{y1} - E_{y0}, E_{z1} - E_{z0}\ ) &= (E_x, E_y, E_z) \end{aligned} \qquad (4)$$

$$\Delta R = (E_x X + E_y Y + E_z Z)/R. \qquad (5)$$

Equation (5) represents the fundamentals of the ballbar measurement. Using this equation, the ballbar results can be correlated with the error vector (E_x, E_y, E_z). This error vector reflects the measured ballbar radius related to the nominal one, expressed as the difference between $\overrightarrow{E_0}$ and $\overrightarrow{E_1}$, and is calculated by the sum of all the machine error parameters in the 3D space, It can be utilized for machine tools and industrial robot error modeling. Conversely, commercial ballbar software uses ΔR as an input to compute machine error parameters such as CD, backlash error, out of squareness, and straightness error.

The general ballbar data analysis process is shown in figure 2. This procedure aligns with the ISO 230-4:2005

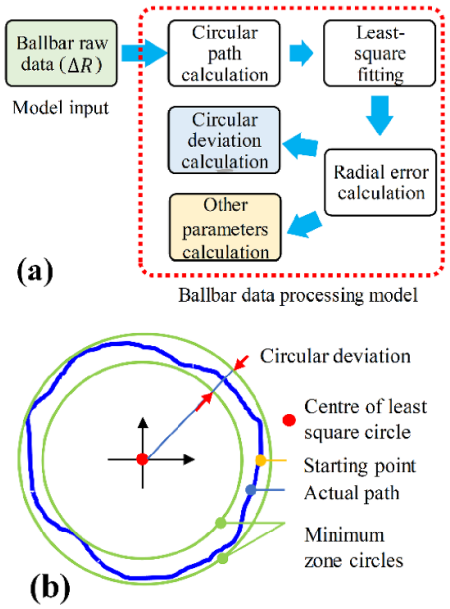

Figure 2. (a) Ballbar data processing flowchart; (b) meaning of CD.

standard [12]. First, the raw data collected from the ballbar were adjusted considering the nominal radius to compute the actual coordinates of the circular trajectory. Following this, the true center of the circular path was identified using a least-squares fitting method. Concurrently, the radial distances between the actual circular path positions and their true centers were calculated. The subsequent step involved determining the radial error, which was defined as the discrepancy between the measured and nominal ballbar radii. Finally, the range of variation of the radial error was computed to quantify the CD [25]. In addition to the radial deviation, other parameters such as backlash, straightness error, and out-of-squareness can be calculated using commercial ballbar software. For more details, please refer to [26].

3. Updated ballbar data processing method

In the present work, following the acquisition of the ballbar raw data, it underwent refinement through the application of the UKF and PSO methods, as illustrated in figure 3. UKF processing is designed to preserve the frequency components that are crucial for determining the static error state of the machining platform. The refined data, characterized by reduced DCs, were then analyzed using the standard ballbar processing model. Subsequently, the CD and other machine-error parameters were calculated. A comparative assessment of radial errors and CDs, both before and after the application of PSO-UKF processing, enables the identification of DC. These DCs can subsequently serve as secondary tools to verify the accuracy and effectiveness of the proposed technology.

3.1. Definition of DCs

The DCs on the ballbar are represented by the differences between the original and filtered radial errors by the

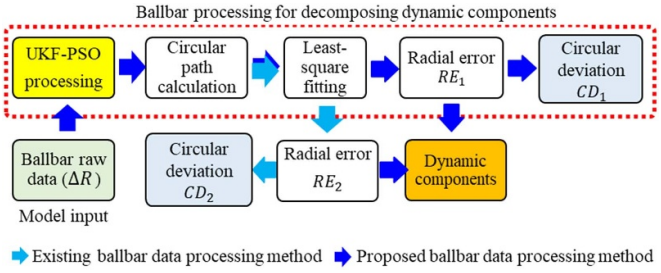

Figure 3. Updated ballbar data processing for decomposing dynamic components.

PSO-UKF. They were quantified by three parameters: (1) differences in CD (DC_1), (2) peak-to-peak value of differences in RE (DC_2), and (3) the mean absolute value of differences in RE (DC_3). The corresponding Eqs of the DCs are processed with MATLAB functions as follows:

$$DC_1 = CD_1 - CD_2, \tag{6}$$

$$DC_2 = \text{peak2peak}\ (RE_1 - RE_2), \tag{7}$$

$$DC_3 = \text{rms}\ (RE_1 - RE_2). \tag{8}$$

3.2. DCs calculation using UKF and PSO

The Kalman filter, established by Rudolf E. Kalman, is an indispensable tool for state estimation in dynamic systems [27]. Although highly effective in systems that exhibit linear relationships, their application is limited in this context. To address this shortcoming, the development of the UKF has been instrumental, providing substantial enhancements [18]. Unlike the conventional Kalman filter, the UKF demonstrates a superior performance in managing nonlinear systems. The UKF further enhances accuracy by eliminating the errors associated with Jacobians and linearization. Its applications extend across various domains including navigation, robotics, economics, and biology. Nonetheless, the UKF, akin to other Kalman filters, requires meticulous tuning, particularly in terms of the noise covariance and scaling parameters.

PSO is versatile, capable of addressing both one-dimensional and multi-dimensional optimization challenges. Configuring PSO for multi-dimensional problems is straightforward, allowing for the integration of additional tuning parameters without fundamentally altering the model. This flexibility makes PSO a method with potential for future enhancements in ballbar data processing. Conversely, alternative methods like Grid Search or GA, which are typically more focused on single-parameter optimization, would necessitate the development of new mathematical models.

Owing to their exceptional efficacy and advantages, both the UKF and PSO have been selected as principal methodologies for the calculation of DCs.

3.2.1. UKF application for ballbar data processing. Given its better ability to approximate Gaussian distributions compared to other nonlinear filters like the extended Kalman

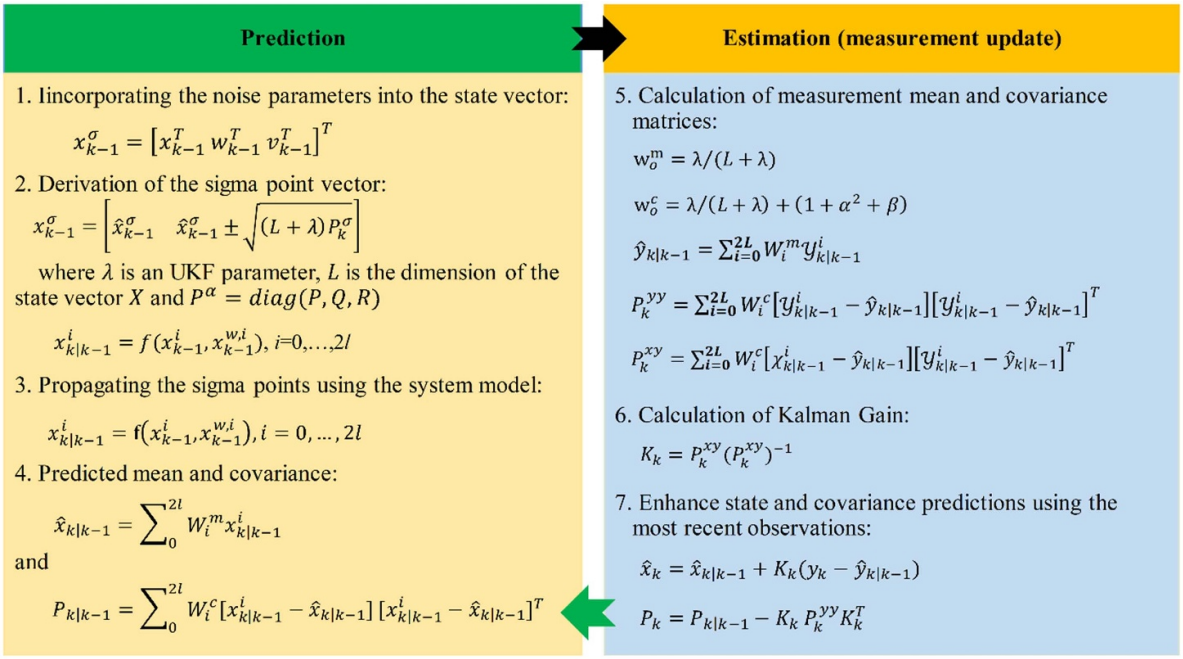

Figure 4. Process of UKF [32].

filter and robust extended Kalman filter, the UKF is chosen as the primary tool for processing ballbar measurements [18].

The steps of the UKF processing are summarized in figure 4. The UKF data processing focuses on two main phases: prediction and estimation (measurement update), which are crucial for state estimation in nonlinear dynamic systems. For the ballbar measurement results, they can be described by equations (9) and (10):

$$X_k = f(X_{k-1}) + w_{k-1}, \tag{9}$$

$$Y_k = f(X_k) + v_k, \tag{10}$$

where k stands for the discrete time step, X_k represents the unobserved state of the ballbar system, which is a known exogenous input, and Y_k is the observed measurement result of the ballbar system.

In the prediction phase, the process noise, denoted as W_k, and the observation noise, V_k are both presumed to be white Gaussian noise processes with the respective covariance matrices Q_k and P_k. When considering the state vector at the $k-1$ step, which has an anticipated mean of $\hat{X}_{k-1}$ and P_{k-1} covariance, the statistics of x_k can be computed by applying the unscented transformation. This involves the calculation of a set of sigma points χ_k^i (a set of strategically chosen sample points used in the UKF to capture the mean and covariance of the state distribution), each paired with corresponding weights W_i. The calculation of sigma points involves the state estimate vector (x) and the state covariance matrix (P). The number of sigma points and their specific values depend on the dimensionality of the state vector (L) and chosen parameters that control the spread of the points.

The spread of the sigma points around the mean state value is controlled by three scaling parameters α, $\bar{k}$ and β. The relationship between α and $\bar{k}$ is connected by an UKF parameter λ which is used in sigma point calculation, expressed as $\alpha^2(L+\bar{k}) - L$. The scaling parameter α (figure 4, step-5), influences the distribution of sigma points around the mean $\bar{x}$ and its typical range lies between 0 and 1. The parameter L stands for the dimension of the state vector and the secondary scaling parameter, $\bar{k}$, was customarily set to zero. As for the parameter λ, it is described in [28–30]. In addition to setting $\bar{k} = 0$, λ could change with α since L is relatively stable for a given state vector. The third scaling parameter β (figure 4, step-5) is employed to integrate prior knowledge regarding the distribution of x, with $\beta = 2$ selected optimal for Gaussian distributions, as substantiated by [31]. Once the predicted state mean and covariance are estimated by the propagated sigma points, process noise is integrated to accommodate uncertainties in system dynamics [30].

In the second phase, the predicted sigma points are processed through the measurement model to estimate expected measurements. The resulting points allow the calculation of the measurement mean and covariance with incorporated measurement noise for observation uncertainties. Subsequently, the Kalman gain is calculated to weigh model predictions against new measurements. Then, the model progressively refines the state estimate by assimilating new observations, thereby improving accuracy iteratively. For a comprehensive understanding of the UKF methodology, the reader is encouraged to consult [30, 32].

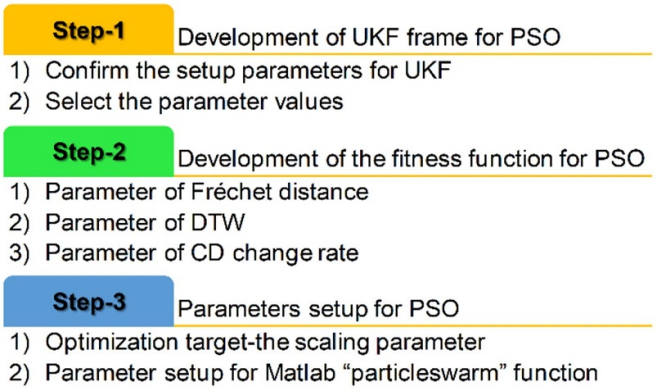

Figure 5. Flowchart for tuning UKF using PSO method for ballbar application.

Based on the above UKF analysis, the key parameters for unscented transformation include λ (affected by α, $\hat{k}$ and L), α, $\hat{k}$ and β. In this work, $\hat{k}$ was selected 0 and β was selected as 2. While α is tuned using PSO method from 1×10^{-5} to 1. For a given dataset, L is fixed, so the tuning of α has the same effect as the tuning of λ. Additionally, tunable factors such as state covariance, process noise, and measurement noise impact UKF performance. These can be selected from literature recommendations or empirically adjusted to meet performance objectives. In this study, based on the data processing results, their values were set to 0.01, 0.001, and 1, respectively.

3.2.2. PSO for UKF tuning. PSO is a general optimization algorithm inspired by the social behavior observed in birds and fish, and it can be effectively applied to both 1-dimensional (single-objective optimization for unimodal or multimodal) and multi-dimensional (multi-objective optimization) problems [20]. PSO processing involves evaluating potential solutions, calculating assessment values, and methodically converging to the global optimum until termination criteria are met. Its suitability for different types of optimization problems depends on the specific characteristics of the problem, such as the complexity of the objective function, the presence of local optima, and the dimensionality of the search space. Employing PSO enhances the ability to uncover diverse parameter sets suitable for the UKF, enabling fine-tuning of the UKF parameters for each ballbar data processing scenario.

A comprehensive visual representation of the PSO workflow for the UKF tuning is shown in figure 5. When applying PSO to a UKF, three primary steps are vital. Firstly, the establishment of the UKF processing frame simplified as equation (11), where BF_n represents the UKF-filtered ballbar data acquired with different conditions, B_n are the ballbar raw data measured under relevant conditions and $x_1, x_2, \ldots, x_{n1}$ are the tunable UKF parameters for example, λ, α, K or β, where $n1$ stands for number of these tunable parameters. The second step involves formulating a fitness function represented as $f(x_1, x_1, \ldots, x_{n1})_n$ (equation (15)). The specifics of this function are described in Eqs from 12 to 14, and n stands for the iterations of the particle when it seeks the optimal solution. Its design mainly relies on three components-two similarity parameters including the Fréchet distance ($\delta_F(BF_n,\ RB_n)$) [33] and the DTW parameter ($DTW(BF_n, RB_n)$) [34], and one parameter indicating the change rate of CD,

$$BF_n = f_{\mathrm{UKF}}(B_n, x_1, x_2, \ldots, x_{n1}) \tag{11}$$

$$\delta_F(BF_n,\ RB_n) = \inf_{p,\sigma} \max_{t\in[0,1]} \|BF_n(p(t)) - RB_n(\sigma(t))\| \tag{12}$$

$$DTW(BF_n, RB_n) = \sqrt{\sum_{(i,j)\in\tau} (BF_n - RB_n)^2} \tag{13}$$

$$CD(n)_{\mathrm{Diff}} = [|CD_F - CD_R| / CD_R] \leqslant 0.1 \tag{14}$$

$$f(x_1, x_2, \ldots, x_{n1})_n = \frac{DTW(BF_n, RB_n) + \delta_F(BF_n,\ RB_n) + CD(n)_{\mathrm{Diff}}}{\sqrt{(DTW(BF_n, RB_n))^2 + (\delta_F(BF_n,\ RB_n))^2 + (CD(n)_{\mathrm{Diff}})^2}} \tag{15}$$

The Fréchet distance (equation (12)) measures the curve similarity by considering both point arrangement and position. In equation (12), p and σ are two reparameterization functions of the unit interval [0,1]. Set t be the time parameter, at time t, the sampling point on curve BF_n is $BF_n(p(t))$, similar for RB_n. p, σ: [0, 1] $\rightarrow$ [0, 1] range over all continuous and non-decreasing functions with $p(0) = \sigma(0) = 0$ and $p(1) = \sigma(1) = 1$ [35]. Ideally, a zero value signifies a perfect curve alignment. Meanwhile, the DTW parameter (equation (13)) evaluates the pattern similarity in the time-series data or between two curves. Again, a zero value indicated a perfect match between the curves. For this equation, τ stands for an alignment path with a length of $k1$ and this path contains $k1$ index pairs $((i_0, j_0), (i_1, j_1), \ldots, (i_{k1-1}, j_{k1-1}))$. To well match the curves of BF_n and RB_n, many admissible paths will be generated and the DTW finds the best alignment between BF_n and RB_n that minimizes the total distance. For a comprehensive understanding of DTW, please refer to [36]. In this context, these two parameters are used to assess the similarity between the UKF-filtered ballbar data and the low feed rate reference ballbar data. A downsampling process was applied to high-speed ballbar measurements to ensure a similar data length to that of the reference ballbar data. In addition, equation (14) introduced the rate of change for CD ($CD(n)_{\mathrm{Diff}}$) which addresses the issue of non-convergence in the optimization function under the selected setup conditions. Successful UKF fitting was indicated when the rate of change is below 0.1. RB_n is the reference data from a slower feed rate, CD_R is the CD measured at a low feed rate, n stands for the number of the iterations for fitness function. Using the three components, fitness function equation (15) is aiming to achieve the global

minimum, which would represent an optimal set of UKF parameters $(x_1, x_1, \ldots, x_{n1})$ that aligns the UKF-filtered ballbar data closely with the reference data (RB_n), ensuring both pattern and curve similarity while maintaining a low rate of change for critical parameters.

The third step covers the parameter setup for PSO method. In this study, the 'particleswarm' function of PSO in MATLAB was utilized to automate the UKF fine-tuning process. The PSO algorithm requires the selection of key parameters, such as the number of tuning targets, their value ranges (minimum and maximum limits), and the self-adjustment and social-adjustment weights. The setup parameters for PSO function 'particleswarm' are as follows: one tuning target of scaling parameter α for the UKF was selected and other tunable parameters, k and β, were chosen as 0 and 2 respectively. Under this configuration, adjusting α is equivalent to adjusting λ, as the dimension of the referenced ballbar data remains constant. It is acknowledged that these selections might potentially affect the performance of the UKF. Nonetheless, in real-world applications, these settings have consistently yielded practical and satisfactory results. In addition, the objective function comprises three primary parameters: the Fréchet distance, the DTW parameter, and the CD change rate. When using Fréchet distance for paths or trajectories similarity processing, an optimization process can indeed encounter multiple local optima while DTW is generally designed to avoid local optima and find a path that represents the global optimum. From this point, the objective function still has the local optima problem. Furthermore, the PSO, developed with this 1-dimensional setup, can be easily extended to more dimensions or to more complex versions of the problem without significant modifications to the optimization algorithm. Therefore, the selection of the tuning target is considered feasible. Based on the components of equation (15), the global best model for PSO was selected because it is better suited for complex, multimodal landscapes where the global optimum is hidden among many local optima. In addition, the number of particles is set as 50, the iterations are selected as 150 and the social adjustment weight is selected as 1.5, respectively. Finally, an indepth study of the PSO can be found in [19].

4. Experimental setup

Movements in the machine components can induce vibrations, thereby affecting the precision of the machining platform. The DCs are influenced by various factors, including feed rate [37], trajectory errors [37] and acceleration/jerk [38]. To investigate the effects of dynamic errors, general ballbar tests were conducted at multiple feed rates in a HMC. Furthermore, ballbar tests under different vibration levels were simulated using the Renishaw simulator, which can replicate testing platforms with diverse error states and varying vibration scenarios. These two sets of data were instrumental in validating the proposed technology.

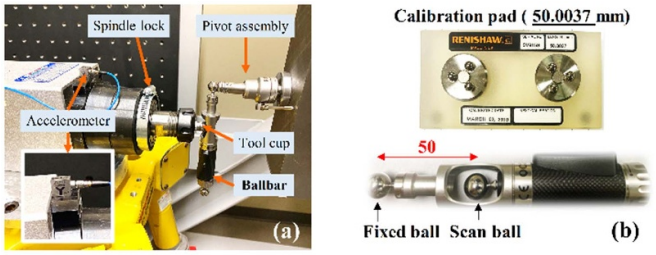

Figure 6. Ballbar measurement setups: (a) a robotic machining cell utilizing industrial hexapods (FANUC F-200iB), (b) a Renishaw ballbar featuring a 50 mm nominal radius.

4.1. Ballbar measurement at HMC

The ballbar test was conducted within a hexapod-based machining cell outfitted with two FANUC F-200iB hexapods, a bench clamp, an electric spindle, and a supporting mechanical frame. The employed Renishaw QC20-W telescopic ballbar boasts an accuracy of 0.1 μm at 20 °C and a measurement range of ±1.0 mm (figure 6(b)) [39]. It was observed that the utilization of this sampling rate configuration in commercial Renishaw software cannot fully capture the complete extent of dynamic errors. Therefore, a custom ballbar data acquisition strategy was developed using Renishaw-provided API and employed for this work, featuring a consistent maximum rate of 1000 Hz.

For the HMC (figure 6(a)), the tool cup was mounted on the electrical spindle of the floor-mounted hexapod, and the pivot assembly magnet base was fixed to the workpiece in the wall-mounted hexapod vise. The scanning balls were connected to a tool cup and pivot assembly. During the ballbar measurement, the hexapod mounted on the floor executed a circular trajectory within the *YZ* plane, whereas its counterpart on the wall remained stationary. Measurements were captured in both CCW and CW movements at the chosen position and speed, with a 1000 Hz sampling rate. For stable ballbar measurements at a consistent feed rate, a 180-degree overshoot was selected to help in achieving the required feed rate and decelerating before feed out [40], as depicted in figure 7. As for the detail of ballbar measurement, please refer to figure A1.

Before the ballbar test, the HMC was preheated by rapidly moving its motors for an hour, a procedure that was consistently followed in all subsequent tests. Given the feed rate of the testing platform, nine typical machining speeds were selected for the ballbar tests: 300, 600, 1200, 1800, 2400, 3000, 3600, 4800, and 6000 mm min^{-1}. Each speed was repeated twice to ensure the accuracy. The ballbar measurements were taken at a randomly chosen position, with the mechanical system's coordinate origin set at [0 mm, 0 mm, 870 mm] relative to the base frame system.

Throughout the ballbar test, vibrations were recorded using a triaxial accelerometer (Model number: 356B21, manufactured by PCB Piezotronics) attached to the electrical spindle. This sensor features a 2048 Hz sampling frequency of 0.125 Hz spectral resolution, and a sensitivity of

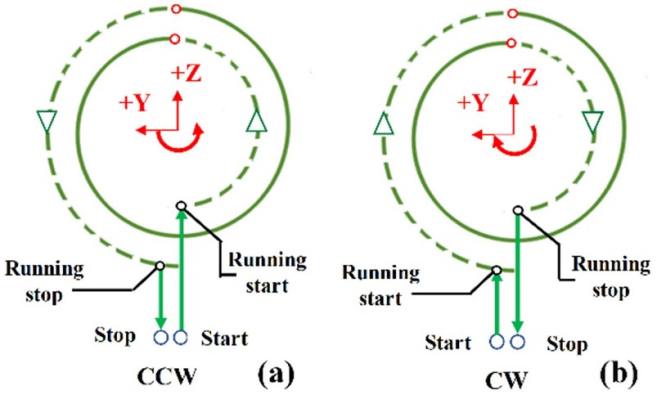

Figure 7. Ballbar measurement techniques: a solid line connects two green dots, symbolizing the arc of ballbar data, while a dotted line links red and black dots, representing the overshoot before and after formal ballbar test. The depiction of a spiral path ensures a circular motion without any overlap, and it is only used for diagrammatic purposes [40]. For the true ballbar measurement, a circular path with a nominally fixed radius was used. In subfigure (a), there is a 180-degree overshoot demonstrated in a counter-clockwise (CCW) direction for ballbar measurement, whereas in subfigure (b), the 180-degree overshoot is shown in a clockwise (CW) direction.

100 mV g^{-1}. The LMS-SCADAS (Model: SCM01) mobile data system was utilized to capture the vibration data, which were subsequently analyzed in the time domain via RMS values.

4.2. Ballbar measurement simulation

The Renishaw software includes a simulation module, the Renishaw Ballbar simulator [41], which generates simulated ballbar data by adjusting parameters, such as test details, geometry errors, play errors, and dynamic errors (figure 8). These parameters can be used to define the accuracy of a virtual testing platform and the simulator allows for the creation of ballbar data with varying dynamic errors, eliminating the need for actual machining tests. The details of these parameters could be found at [40]. The detail flowchart for ballbar data simulation could be found at figure 8. With the exception of the 'Vibration pk-pk' parameter, all other parameters can be selected based on the real ballbar results from an HU-40 T five-axis machine tool (option-1) or randomly selected (option-2). By adjusting the vibration magnitude value (abbreviated as Vib *pk–pk* at the dynamic error interface), simulated ballbar data with varying dynamic errors can be generated.

The selected error parameters for the Renishaw simulator is outlined in appendix tables A and B. To assess the stability of the UKF and PSO, six diverse datasets were chosen for testing. The first four datasets were obtained from actual measurements originating from the HU-40 T five-axis machine tool on different days under various conditions. The remaining two datasets were randomly selected. For the six dataset, the Vib *pk–pk* varied as 0, 5, 10, and 15 μm were selected.

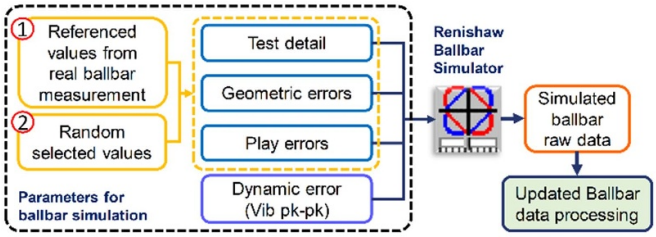

Figure 8. Flowchart for ballbar measurement simulation. Two options could be used for non-dynamic-error-parameter selection.

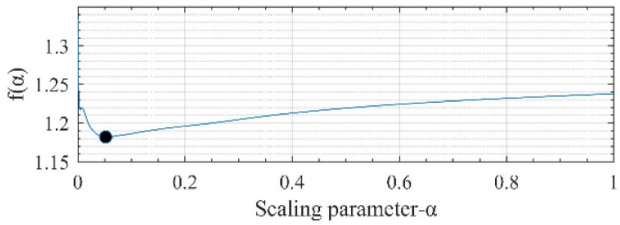

(a) Correlation between scaling parameter and target function

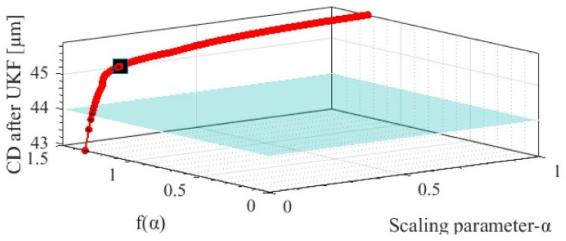

(b) Interrelation between scaling parameter, objective function, and CD

Figure 9. Relationship between the scaling parameter, target function and CDs, and the blue dot of figure (a) stands for the optimal scaling parameter and the light blue plane stands (b) for the control limit (decided by equation (14) for CD).

5. Results and analysis

5.1. PSO-UKF processing for ballbar measurement

According to the Renishaw guidelines, lower feed rates are optimal for measuring the geometric errors. Consequently, the ballbar data obtained at a feed rate of 300 mm min^{-1} served as a reference for subsequent PSO analysis. The results captured at a speed of 1200 mm min^{-1} were employed to demonstrate the effectiveness of the proposed UKF and PSO methods for DC calculations. The value of the target function decreased with the scaling parameter. The local minimum was found at a value close to 1. Meanwhile, under the range of scaling parameter of 0–1 with the interval of 1×10^{-5}, the change range of CD was around1.5 μm (figure 9). For this case, the scaling parameter was selected as 0.0442, and the CD values before and after UKF were 46 μm and 45 μm, respectively. This change indicates the effect of DCs on CD. Using the same data processing, the CDs of the ballbar measured at different feed rates containing fewer DCs can be calculated.

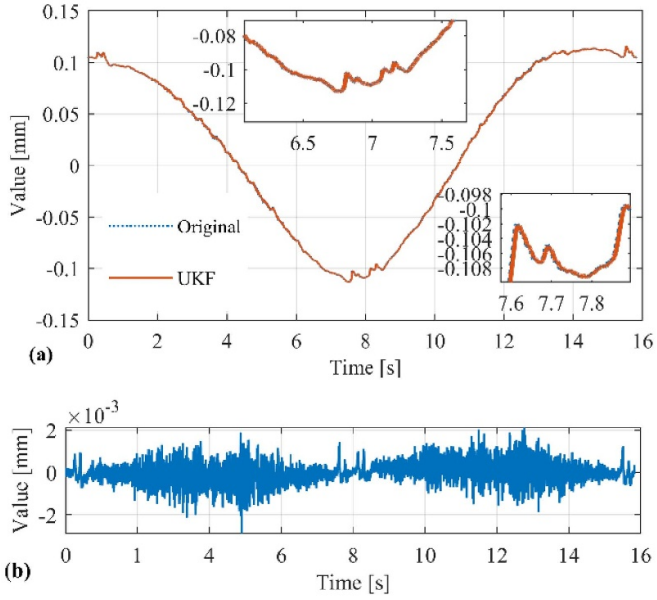

Figure 10. (a) Ballbar raw data measured with feed rate of 1200 mm min^{-1} before and after UKF filtering; (b) differences of ballbar raw data before and after UKF processing.

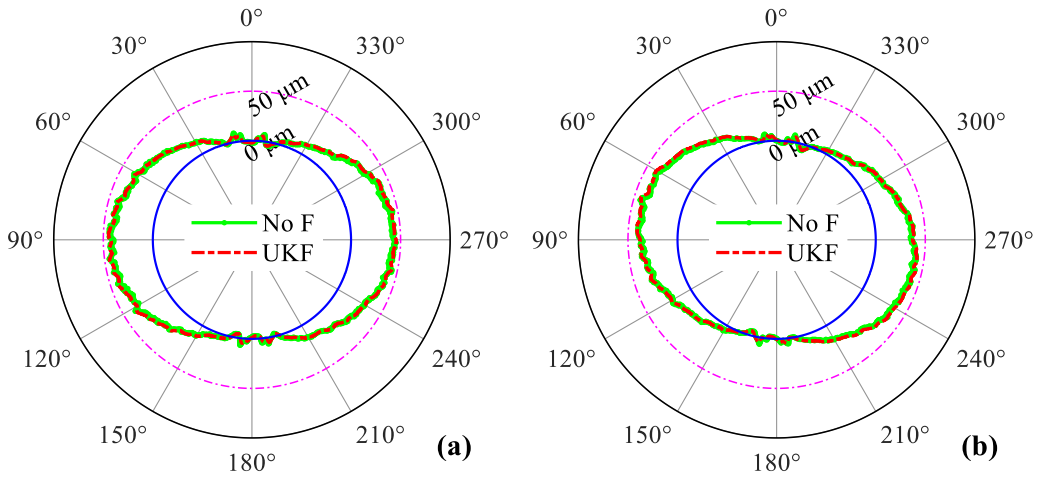

Figure 11. Radial error patterns of hexapod (floor) at a feed rate of 1200 mm min^{-1} at the CCW (a) and CW (b) direction, No F stands for the none filtering operation for the ballbar raw data.

5.2. Results of ballbar measurement from HMC

Considering the measurement precision and efficiency, the ballbar results at this speed were used to showcase the general processing results of the proposed UKF (figure 10). To show the differences before and after UKF processing, the difference of the ballbar raw data before and after UKF was calculated (figure 10(b)) and the maximum difference was found to be than 3 μm. In addition, the main shape of the ballbar raw data is well preserved after filtering. The radial error curves in the CCW and CW directions also maintained their main curve shapes after filtering (figure 11), indicating the minimal dynamic errors was found at a feed rate of 1200 mm min^{-1}. The impact of the DCs on the ballbar results is shown by the calculated parameters DC_1, DC_2, and DC_3 in figure 12. It is theorized that dynamic errors can be influenced by feed rate. The optimal indicator for DCs should exhibit smaller values compared to the CDs, and should increase with higher feed rates. After filtering, DC_1 and DC_3 both accounted for 5% of the CDs measured with the highest feed rate, while DC_2 represented approximately 87% of that of CD. Remarkably, a relatively stable increasing tendency was observed with DC_1 when measuring feed rates of 1800 and 2400 mm min^{-1}, but DC_2 and DC_3 at these speeds clearly demonstrated distinct dynamic characteristics (see figures 12(c) and (d)). Consequently, DC_3 performed better than DC_1 in capturing DCs in ballbar measurements. Ultimately, these results validate the effectiveness of the proposed method for calculating DCs. Because the DC is closely related to the vibration, the proposed method was

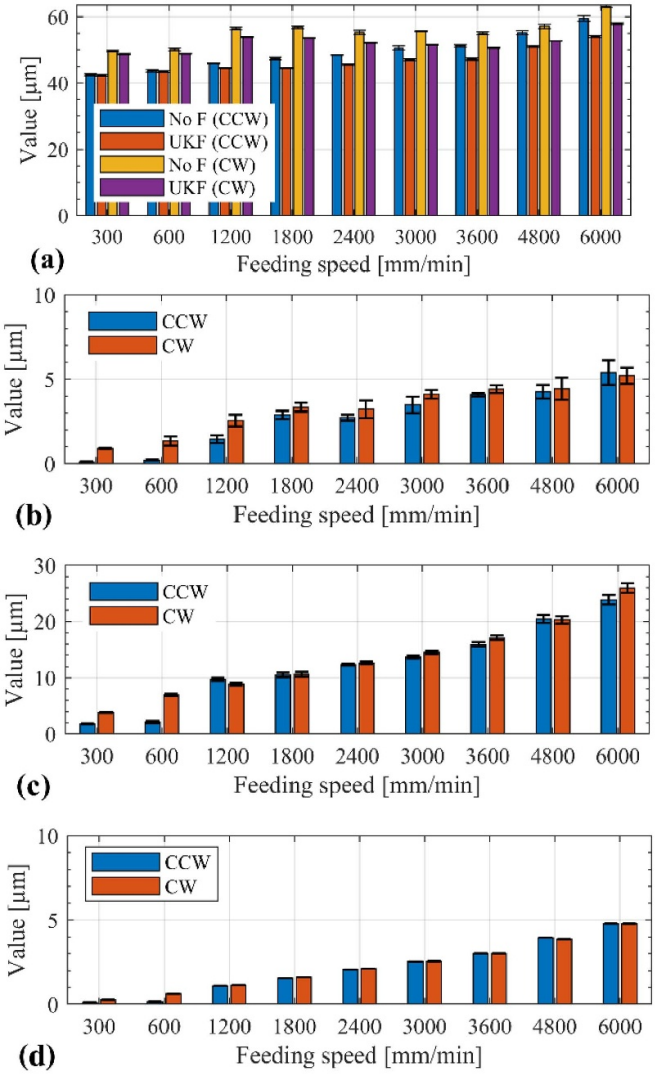

Figure 12. CDs and DCs of ballbar measured with different feed rates in the CCW and CW directions before and after UKF processing, (a) CDs of ballbar tests measured with different feed rates, DC_1, DC_2, and DC_3 of ballbar measurement using the proposed PSO-UKF are shown at (b)–(d), respectively.

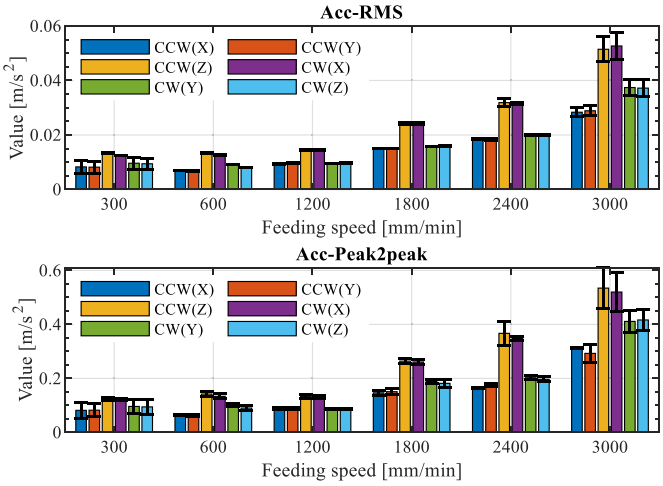

Figure 13. Vibration signal statistical results (X, Y, and Z axes) during ballbar measurement at varying feed rates.

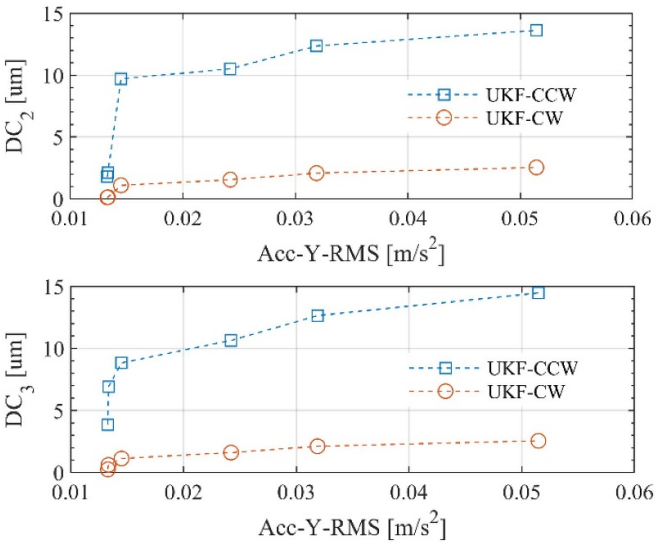

Figure 14. Relationship between DC_2/DC_3 and RMS of acceleration measured at the Y-axis direction under feed rate from 300 to 3000 mm min^{-1}.

also validated by analyzing the synchronous vibration tests during ballbar measurements. The statistical results of the vibration data during the ballbar tests, as shown in figure 13, reveal a clear upward trend in the RMS and Peak2peak parameters.

It is worth noting that the results presented in figures 10 and 11 appear similar, a similarity attributable to the relative relationship between the DCs and the CDs. During ballbar measurements at low feed rates, the DCs are comparatively minor but increases with the feed rate. A peak in the DC is observed at a feed rate of 6000 mm min^{-1}, as illustrated in figure 12.

Figure 14 illustrates the correlation between the acceleration and DC_2/DC_3. A clear upward trend can be seen in DC_2 and DC_3 processed using the UKF when the feed rate is over 1200 mm min^{-1}. This result indicates the efficiency of the proposed filtering technology in determining the impact of DCs on ballbar results. However, the accuracy of the proposed method cannot be determined based solely on the ballbar results obtained at varying feed rates.

Figure 15 presents a statistical comparison of CDs measured at different feed rates before and after UKF processing. The mean and standard deviation (SD) of all the CDs were calculated. Post-PSO-UKF processing shows reduced CDs in the CCW and CW directions (figure 15(a)). This means that the DCs were decomposed by general ballbar processing. A lower SD value indicates an enhanced stability during the ballbar measurement process with the UKF. For varying feed rates, the SDs of the CDs were below 1 μm, with a clear reduction in SDs after UKF processing as the feed rate increased (figure 15(b)).

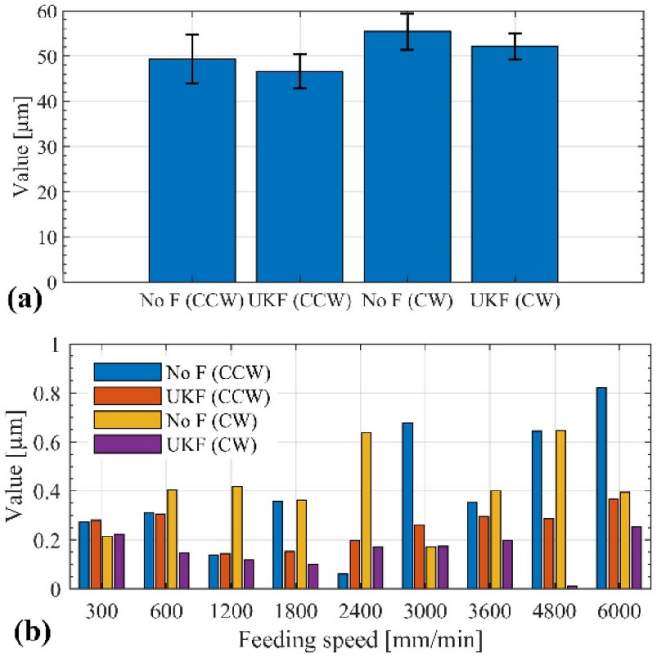

Figure 15. Statistical analysis of CDs (a, mean of CDs and b, SDs) of measurements before and after PSO-UKF processing.

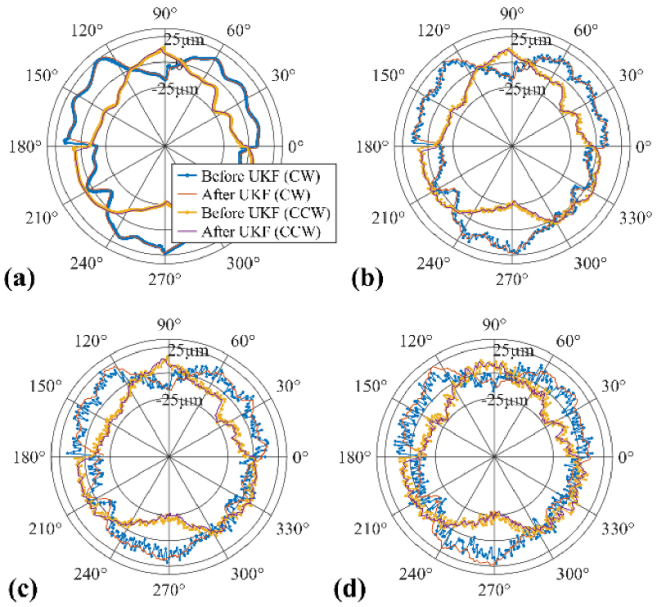

Figure 16. Comparison of radial error curve pattern before and after UKF processing in simulation 1, (a) Vib pk–pk = 0 μm; (b) Vib pk–pk = 5 μm; (c) Vib pk–pk = 10 μm; (d) Vib pk–pk = 15 μm.

Therefore, the stability of the ballbar measurement results can be improved using the proposed method.

5.3. Results of simulated ballbar measurement from Renishaw simulator

Figure 16 illustrates the radial error curve pattern obtained from the simulated ballbar data (simulation 1) before and after the UKF processing. Despite varying the Vib *pk–pk* values, the main shapes of the radial deviation curves with different vibration magnitudes were well preserved after UKF processing (figure 16).

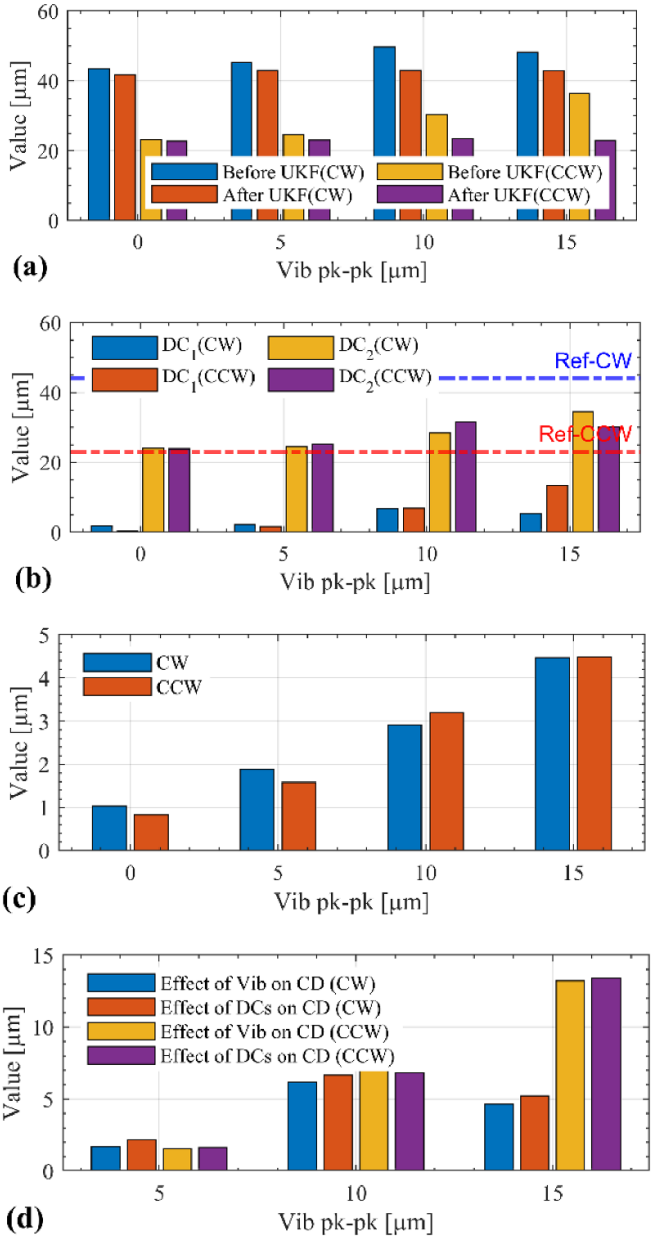

Figure 17. Comparison of CD and DCs parameters before and after UKF in the simulation 1, (a) CDs of ballbar tests, (b) DC_1 and DC_2 of ballbar measurement, (c) DC_3 of ballbar measurement and (d) effects of Vib and DCs on CDs.

The CDs of the CW and CCW directions are comparable to the CD measured at Vib *pk–pk* = 0 μm, with a maximum difference of 1.6 and 1.7 μm respectively (figure 17). DCs increased with vibration. However, the DCs did not change in sync with the input vibration (figures 17(b) and (c)), indicating that the simulated vibration did not have the same effect as the extracted DCs on the CD. This was validated using the Renishaw ballbar simulator. The change in CD under various

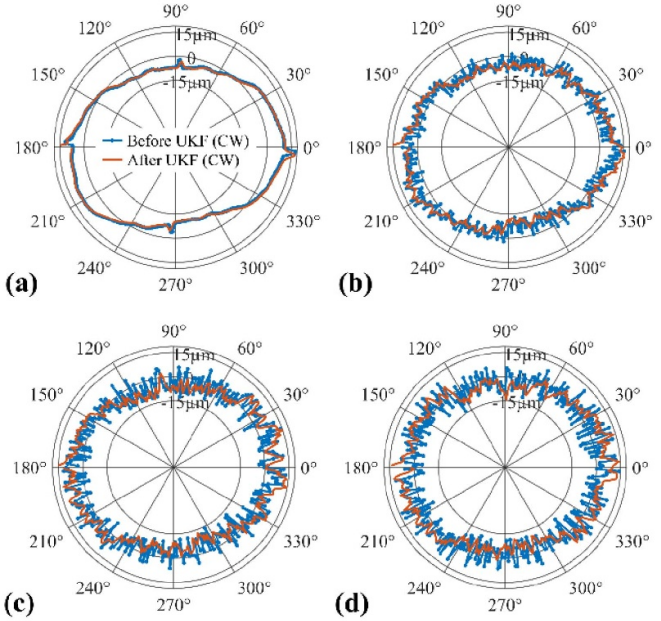

Figure 18. Comparison of radial error curve pattern before and after UKF processing in simulation 2, (a) Vib pk–pk = 0 µm; (b) Vib pk–pk = 5 µm; (c) Vib pk–pk = 10 µm; (d) Vib pk–pk = 15 µm.

vibrations relative to the CD measured at zero vibration was also calculated and is referred to as the effect of vibration on CD. Ideally, this change should match the DC parameters if the UKF performs optimally. Figure 17(d) shows the effect of vibration and DCs on the CDs in the CW and CCW directions. The effect of the vibration and DCs on the CD was close to the maximum differences of 1.6 µm. This slight change may have been caused by the selection of parameters in the UKF. Similar results were obtained in simulation 5 (appendix figures B5 and B6).

The results of simulation 2 showed a change in the radial error curve pattern as the vibration states increased from 5 to 15 µm (as depicted in figure 18). This deviation was significantly different from the pattern observed in Simulation 2 with no vibrations. After undergoing UKF processing, the CD for vibration states between 5 and 10 µm remained close but saw a marked change for states of 15 µm. On the other hand, the DCs showed an increase with increasing vibration states (as shown in figures 19(b) and (c)). There were notable changes in the impact of DCs and vibration on the CDs (as seen in figure 19(d)), especially for the vibration state of 15 µm. This indicates that the UKF still has the ability to extract dynamic effects, but struggles to accurately capture the DCs present in the ballbar results.

The UKF ballbar data processing produced similar results in simulation 6. Unlike simulation 2, the machine error parameters in simulation 6 were randomly chosen, and the number of readings per full circle was increased from 360 to 1000. This resulted in the acquisition of more data for each circular movement. The radial error curve pattern in figure 20 mostly remained consistent with Vib *pk–pk* values of less than

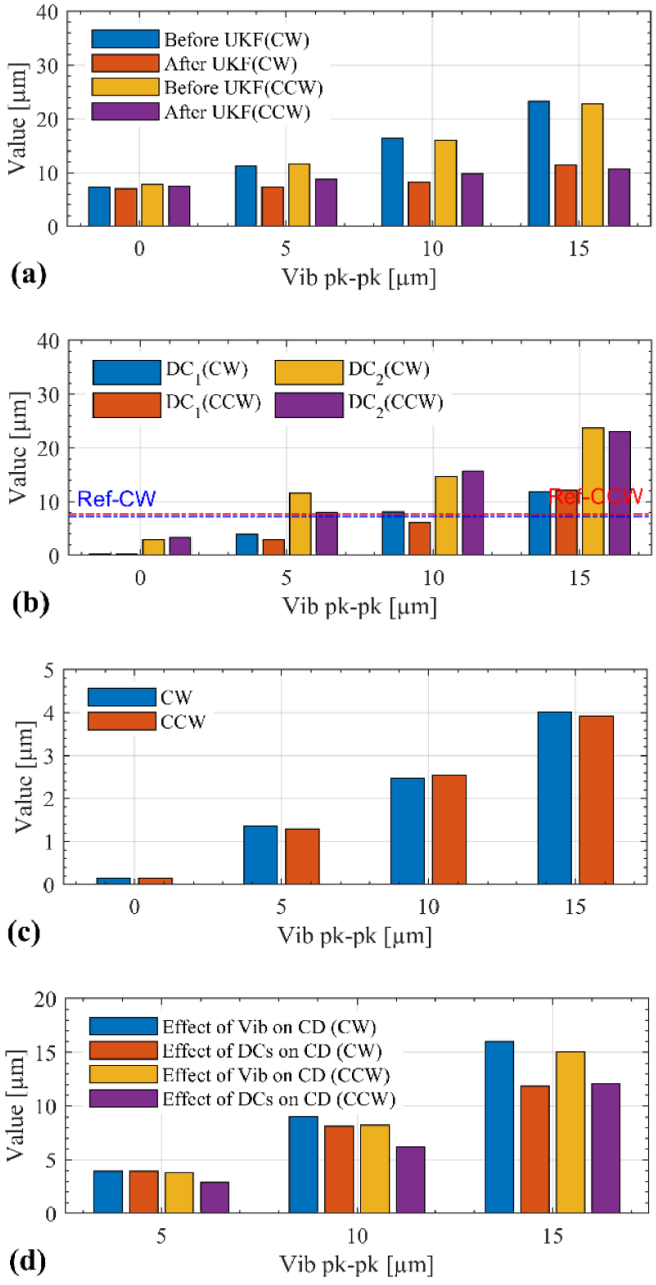

Figure 19. Comparison of CD and DCs parameters before and after UKF in the simulation 2, (a) CDs of ballbar tests, (b) DC_1 and DC_2 of ballbar measurement, (c) DC_3 of ballbar measurement and (d) effects of Vib and DCs on CDs.

10 µm, but significant changes were observed at a Vib *pk–pk* value of 15 µm.

After UKF processing, the CDs of the simulated ballbar data with Vib *pk–pk* less than 15 µm were consistent (figure 21(a)). The DCs increased with the Vib *pk–pk* values (figures 21(b) and (c)), demonstrating that UKF still effectively extracts DCs from the ballbar results. A similar effect of vibration and DCs on CDs was observed at Vib *pk–pk* values ranging from 5 to 15 µm (figure 21(d)), indicating that UKF

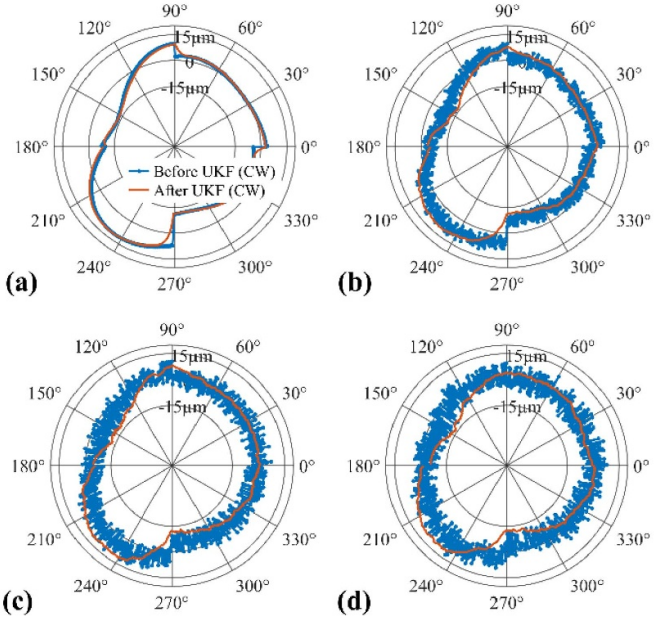

Figure 20. Comparison of radial error curve pattern before and after UKF processing in simulation 2, (a) Vib pk–pk = 0 μm; (b) Vib pk–pk = 5 μm; (c) Vib pk–pk = 10 μm; (d) Vib pk–pk = 15 μm.

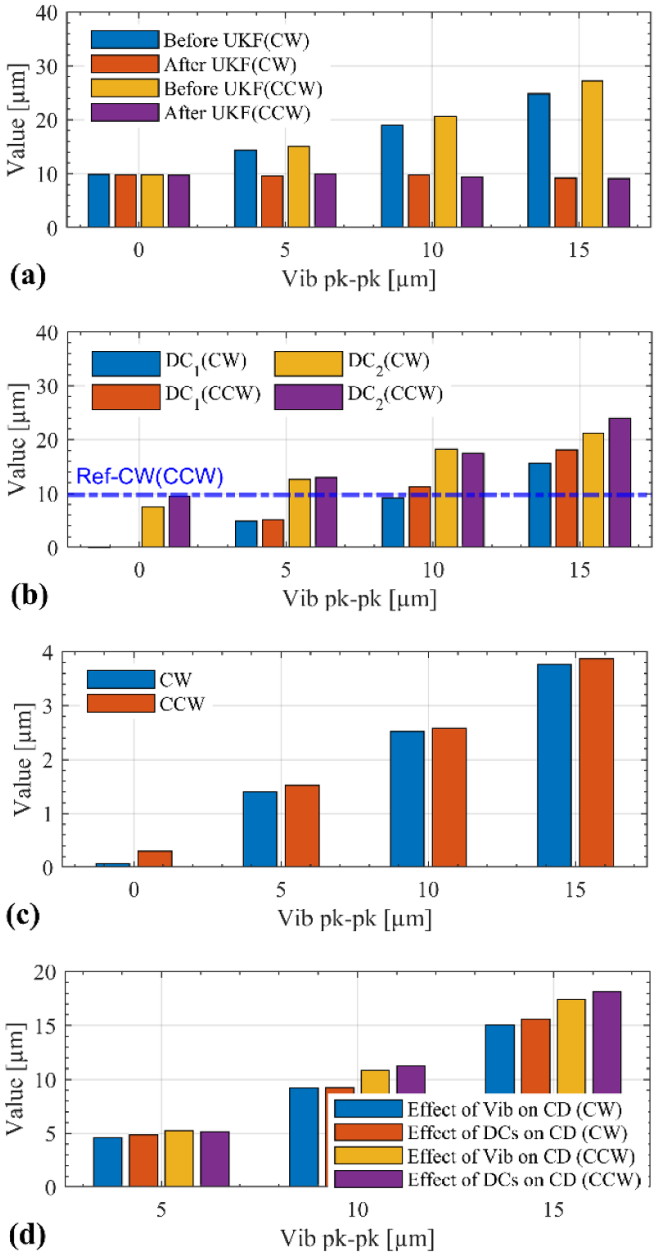

Figure 21. Comparison of CD and DCs parameters before and after UKF in the simulation 2, (a) CDs of ballbar tests, (b) DC_1 and DC_2 of ballbar measurement, (c) DC_3 of ballbar measurement and (d) effects of Vib and DCs on CDs.

has stable precision in processing simulation data with Vib *pk–pk* values less than 10 μm. However, when the Vib *pk–pk* values become too high, the UKF performance decreases. Comparing simulations 2 and 6, we found that the CDs of the primary data with zero vibration were smaller than those with added vibration, and that the number of readings per full circle was different.

Despite these differences, the UKF performed similarly in both the simulations. When the vibration is less than the primary CD value, DCs can be accurately calculated; however, when the vibration exceeds the primary CD value, UKF's performance of the UKF in ballbar data processing decreases. However, using a higher number of readings per full circle may result in a slight improvement in the UKF performance. The validity of the findings was confirmed through simulations 3 and 4 (as shown in appendix figures B1–B4. Both simulations used the same machine error setup, but simulation 4 had a higher number of readings on a full circle (1000) than simulation 3 (360). The processing results for both simulations are presented in appendix figures B3 and B4. Simulation 4 demonstrated better preservation of the radial error curve pattern under various vibration states than simulation 3. It was noted that for simulation 3, the actual radial error curve pattern deviated slightly from the pattern measured under zero vibration owing to the limited number of readings. However, the UKF processing in simulation 4 showed an improved performance with CDs closer to the zero-vibration measurement. The results also showed that the UKF performance can be improved by increasing the number of readings or the sampling rate. Furthermore, when the dynamic errors expressed through vibration are smaller than those in the normal ballbar test CD, the UKF performs better. However, when the vibration is significantly large, the performance of the UKF is variable, and the impact of DCs on the ballbar measurement cannot be accurately determined.

6. Discussion

As the main components of the updated ballbar processing method, the performance of the UKF and PSO in reducing dynamic errors was validated with experimental ballbar data

from the HMC and simulated data from the Renishaw ballbar simulator. The proposed technology was evaluated using the following criteria. First, the radial error curve pattern before and after the UKF processing was evaluated using the fitness function. Second, the correlation between the DCs and the vibrations related to feed rates and Vib *pk–pk* for the simulation setups was evaluated. Finally, the CDs before and after the UKF processing were compared. Using the proposed technology, the radial error curve displayed consistent patterns in both the pre- and post-UKF processing. DCs rose in sync either because of vibrations in the ballbar measurement or because of the Vib *pk–pk* in the simulation. Additionally, the fitted ballbar results closely matched our reference (measured at a feed rate of 300 mm min^{-1}), confirming the effectiveness of the UKF and PSO in reducing DCs at high feed rates. After the UKF and PSO processing of real ballbar data taken at various feed rates, both the mean and standard deviation of the results significantly decreased compared to the original data. A reduced standard deviation indicates a more stable ballbar measurement.

However, the performance of the UKF and PSO can vary based on factors such as the target function, ballbar measurement sampling rate, and the relationship between DCs and the machine's accuracy state. The target function value was expected to converge as a single scaling parameter. However, as demonstrated in this study, ballbar measurements may not always converge in this manner. Therefore, a secondary condition, expressed by equation (14), was used to select the optimal scaling parameter. A scaling parameter smaller than the optimal value can still be effective, resulting in only a minor change in the final CDs value. Given this minimal impact, slight adjustments to the scaling parameter did not significantly affect the reduction in DCs in the ballbar results. Given a similar relationship between DCs and the accuracy state of the machine, simulations 3 and 4 demonstrate that a higher sampling rate enhances the reduction of DCs in the ballbar results. The simulation tests clearly highlight the significance of the relationship between DCs and the accuracy state of the machine. If the DCs exceed the accuracy level of the machine (represented by CD), the proposed UKF and PSO might not completely extract the DCs from the ballbar results. The lower the DCs, the better the performance of the UKF and PSO. For ballbar tests conducted at feed rates between 300 and 6000 mm min^{-1}, the calculated DCs were minimal with a peak of 6 μm (represented by DC_1). This is much smaller than the referenced CD at a feed rate of 300 mm min^{-1}, indicating that the UKF- and PSO-based ballbar processing methods performed effectively at these feed rates. Therefore, by selecting the optimal target function and higher sampling rate, the proposed method can achieve better performance. Furthermore, expanding the optimization scope to include all scaling parameters α, κ, and β presents a potential avenue for future work.

To implement the proposed methodology on a new testing platform, a reference ballbar measurement with a low feed rate is essential because it can serve as a baseline for scaling parameter selection when the target function does not converge. The choice of this feed rate can be referenced by the findings of this study, which identified a minimal DC value at approximately 300 mm min^{-1} or even smaller. The ballbar measurement captured fewer DCs when a lower feed rate was employed. While a ballbar with a radius of 50 mm yields an acceptable measurement time, a larger ballbar radius (e.g. 100–400 mm) results in a substantial increase in the measurement time. To enhance ballbar measurement efficiency and precision, a relatively higher feed rate might be preferred in ballbar measurements, where the suggested methodology can be applied. Furthermore, understanding the DCs of typical ballbar measurements is essential. The existing commercial ballbar processing tools lack this capability, whereas the proposed ballbar processing method can directly address this limitation. Finally, as a dependable method for decomposing DCs, analyzing the dynamic aspects arising from a machine's regular movements can provide valuable insights into its relationship with machine design and maintenance.

7. Conclusion and future work

This study proposed an updated ballbar processing method to decompose the DCs contained in ballbar measurements using the UKF and PSO methods. This is helpful for minimizing the dynamic errors contained in normal ballbar tests under different feed rates. The effectiveness of the proposed technology was verified using real experimental data obtained from the HMC and simulated ballbar data generated using a Renishaw ballbar simulator. Experimental ballbar tests were performed at various feed rates. The dynamic error in the simulated data was modeled with the peak-to-peak vibration (Vib *pk–pk*) ranging from 0 to 15 μm, and the other machine parameters were either based on measurements from the HU40-T machine tool or selected randomly. The results of the experimental and simulated ballbar tests yielded the following conclusions.

1. The DCs extracted from the ballbar results using PSO-UKF demonstrate a synchronized rise corresponding to the vibration levels observed at different feed rates. Consequently, the PSO-UKF offers a potential solution for comprehending and decomposing the DCs within standard ballbar measurements.
2. The proposed updated ballbar processing method, based on the UKF and PSO methods, can effectively reduce the DCs in ballbar measurements taken at varying feed rates. This enhances both efficiency and precision, especially at higher feed rates for ballbar measurements. As a universal approach, it is applicable for ballbar tests across different manufacturers and testing machines.

3. The performance of the UKF and PSO in processing ballbar data can be improved by selecting the optimal target function of the PSO and sampling rate of the ballbar. A higher sampling rate can enhance the precision of the ballbar measurements measured at a higher feed rate.

For the next step of this work, the performance of the proposed method is verified using data measured from general machine tools. The DCs extracted using our proposed method for scheduling the maintenance of the machining platform are also considered. Additionally, expanding the optimization target to include all scaling parameters, α, $\bar{k}$, and β, could potentially enhance the performance of both UKF and PSO.

Data availability statement

The data cannot be made publicly available upon publication due to legal restrictions preventing unrestricted public distribution. The data that support the findings of this study are available upon reasonable request from the authors.

Acknowledgments

The authors express their gratitude for the financial support received from the Fonds de recherche du Québec—Nature et Technologies (FRQNT) through a postdoctoral research scholarship and the Natural Sciences and Engineering Research Council of Canada (NSERC).

Appendix

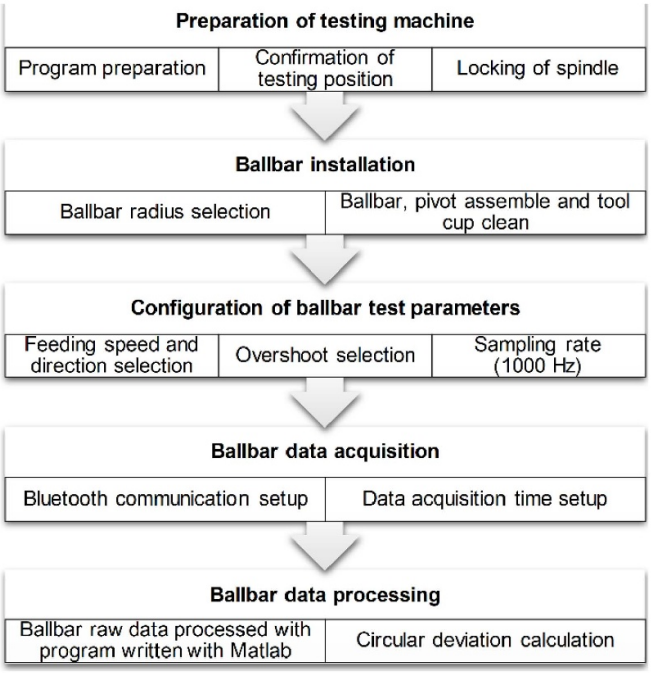

Figure A1. Flowchart for ballbar measurement at the hexapod machining cell.

Owing to the close proximity of the radial error curve patterns in the CW and CCW directions for Simulations 3, 4, and 5, only the CW pattern is presented for clarity.

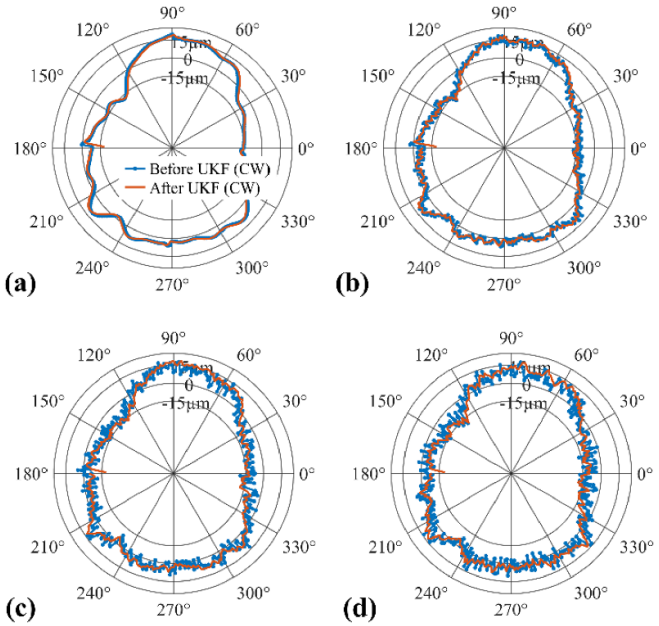

Figure B1. Comparison of radial error curve pattern before and after UKF processing in simulation 3, (a) Vib *pk–pk* = 0 μm; (b) Vib *pk–pk* = 5 μm; (c) Vib *pk–pk* = 10 μm; (d) Vib *pk–pk* = 15 μm.

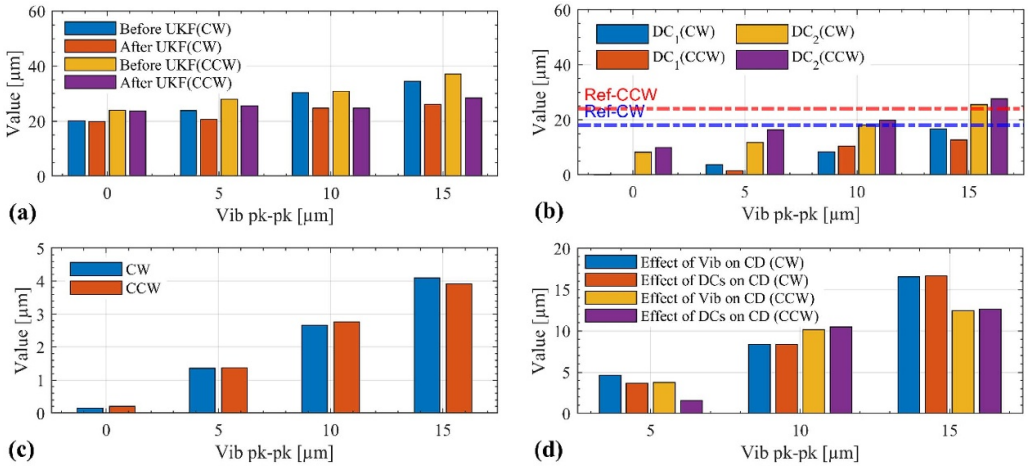

Figure B2. Comparison of CD and DCs parameters before and after UKF in the simulation 3, (a) CDs of ballbar tests, (b) DC_1 and DC_2 of ballbar measurement, (c) DC_3 of ballbar measurement and (d) effects of Vib and DCs on CDs.

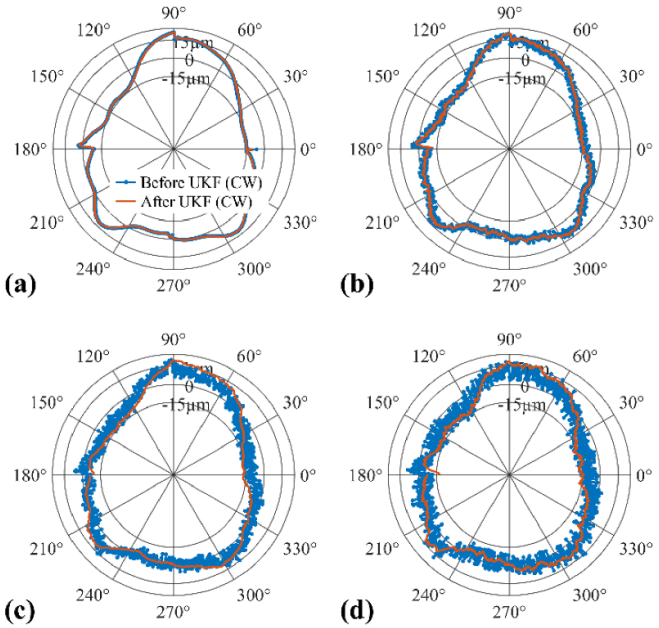

Figure B3. Comparison of radial error curve pattern before and after UKF processing in simulation 4, (a) Vib *pk–pk* = 0 μm; (b) Vib *pk–pk* = 5 μm; (c) Vib *pk–pk* = 10 μm; (d) Vib *pk–pk* = 15 μm.

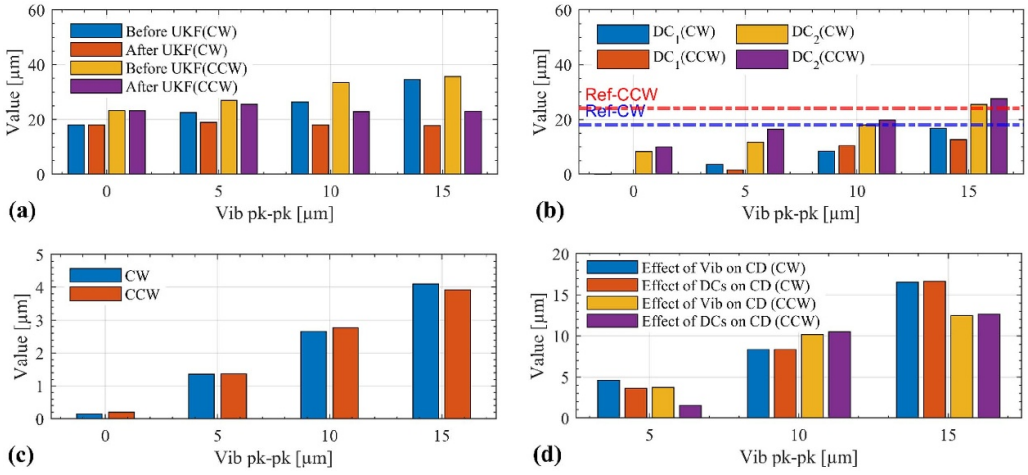

Figure B4. Comparison of CD and DCs parameters before and after UKF in the simulation 4, (a) CDs of ballbar tests, (b) DC_1 and DC_2 of ballbar measurement, (c) DC_3 of ballbar measurement and (d) effects of Vib and DCs on CDs.

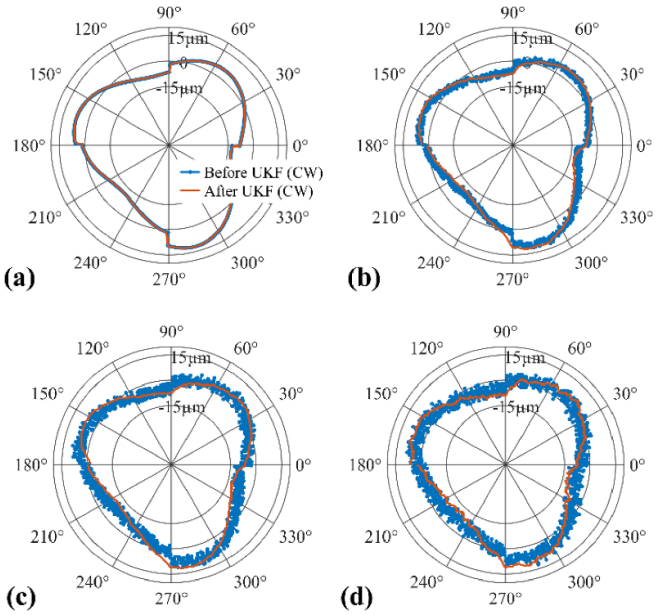

Figure B5. Comparison of radial error curve pattern before and after UKF processing in simulation 5, (a) Vib *pk–pk* = 0 μm; (b) Vib *pk–pk* = 5 μm; (c) Vib *pk–pk* = 10 μm; (d) Vib *pk–pk* = 15 μm.

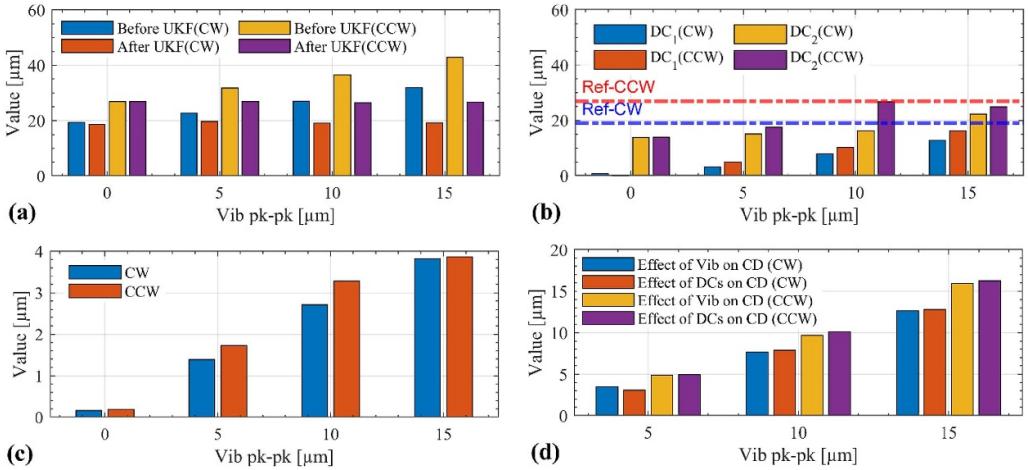

Figure B6. Comparison n of CD and DCs parameters before and after UKF in the simulation 5, (a) CDs of ballbar tests, (b) DC_1 and DC_2 of ballbar measurement, (c) DC_3 of ballbar measurement and (d) effects of Vib and DCs on CDs.

Table A. Setup of machine error parameters for the Renishaw ballbar simulator.

Main items	Parameters	Simulation-1	Simulation-2	Simulation-3	Simulation-4	Simulation-5	Simulation-6
Test details	Feed rate (mm min^{-1})	1001	998	998.6	1000	100	100
	Test radius (mm)	50	150	150	150	100	100
	Number of readings in a full circle	360	360	360	1000	1000	1000
Geometry errors	Scaling error-*x* (ppm)	−36.5	18.3	−30.5	−30.5	−36	−18
	Scaling error-*y* (ppm)	−15.3	−16.4	26.9	26.9	8	8
	Squareness	16.2	−15.8	−24.3	−24.3	−32	28
	Straightness-*X*	−16.8	−1.8	−19.4	−19.4	18	−8
	Straightness-*Y*	2.0	−0.5	8.7	8.7	−24	2
	Cyclic error-*X* (μm)	3.9 (right) 5.8 (left)	0.9 (right) 0.8 (left)	3.7 (right) 6.0 (left)	3.7 (right) 6.0 (left)	0	0
	Cyclic error-*Y* (μm)	13 (up) 5.9 (down)	0.8 (up) 0.6 (down)	6.2 (up) 2.5 (down)	6.2 (up) 2.5 (down)	0	0
	Cyclic pitch-*X* (mm)	12	38.1	50	50	0	0
	Cyclic pitch-*Y* (mm)	18	44.45	50	50	0	0
Play errors	Backlash-*X* (μm)	−5.2 (right) 11.1 (left)	0.1 (right) 0.7 (left)	−0.3 (right) 5.6 (left)	−0.3 (right) 5.6 (left)	4 (right) −5 (left)	1 (right) −3 (left)
	Backlash-*Y* (μm)	1.9 (up) 4.2 (down)	−0.2 (up) 0 (down)	−2.4 (up) −0.6 (down)	−2.4 (up) −0.6 (down)	5 (up) −8 (down)	−3 (up) 7 (down)
	Backlash compensation-*X* (μm)	0	0	0	0	0	0
	Backlash compensation-*Y* (μm)	0	0	0	0	0	0
	Lateral play-*X* (μm)	7.3 (right) 14.1 (left)	−1.4 (right) 1.1 (left)	15.5 (right) −6.2 (left)	15.5 (right) −6.2 (left)	0	0
	Lateral play-*Y* (μm)	−64.2 (up) 58.2 (down)	−0.2 (up) 0.4 (down)	9.4 (up) 1 (down)	9.4 (up) 1 (down)	0	0
Dynamic errors	Vibration *pk–pk* (μm)	0/5/10/15	0/5/10/15	0/5/10/15	0/5/10/15	0/5/10/15	0/5/10/15
	Servo mismatch (ms)	0.02	0	0.22	0.22	0	0
	Reversal spikes-*X* (μm)	4.0 (right) 3.1 (left)	2.5 (right) 1.1 (left)	−1.3 (right) 2.4 (left)	−1.3 (right) 2.4 (left)	0	0
	Reversal spikes-*Y* (μm)	3.2 (up) −2.2 (down)	1.8 (up) 1.8 (down)	1.1 (up) 1.6 (down)	1.1 (up) 1.6 (down)	0	0

Table B. Setup of machine error parameters for the Renishaw Ballbar Simulator.

Main items	Simulation-1	Simulation-2	Simulation-3	Simulation-4	Simulation-5	Simulation-6
Circular deviation (CD) (μm)	43.5 (CW) 43 (CCW)	7.3 (CW) 7.8 (CCW)	20 (CW) 24 (CCW)	18 (CW) 23 (CCW)	36.5 (CW) 48.8 (CCW)	9.8 (CW) 9.77 (CCW)

ORCID iD

Zhaoheng Liu https://orcid.org/0000-0002-8088-7136

References

[1] Yang S-H, Kim K-H and Park Y K 2004 Measurement of spindle thermal errors in machine tool using hemispherical ball bar test *Int. J. Mach. Tool Manuf.* **44** 333–40

[2] Schwenke H, Knapp W, Haitjema H, Weckenmann A, Schmitt R and Delbressine F 2008 Geometric error measurement and compensation of machines-An update *CIRP Ann.-Manuf. Technol.* **57** 660–75

[3] Bryan J B 1982 A simple method for testing measuring machines and machine tools part 1: principles and applications *Precis. Eng.* **4** 61–69

[4] Holub M, Jankovych R, Vetiska J, Sramek J, Blecha P, Smolik J and Heinrich P 2020 Experimental study of the volumetric error effect on the resulting working accuracy—roundness *Appl. Sci.* **10** 6233

[5] Wang W, Sun T, Chen Z, Wu H, Lu K, Wang C, Xu K, Sang Z, Yang H and Shi G 2022 Telescopic ball bar with an indexing joint for measuring machine tool error *Meas. Sci. Technol.* **33** 105904

[6] Dassanayake M, Yamamoto K, Tsutsumi M, Saito A and Mikami S 2008 Simultaneous five-axis motion for identifying geometric deviations through simulation in

machining centers with a double pivot head *J. Adv. Mech. Des. Syst. Manuf.* **2** 47–58
[7] Sun T, Wang W, Wang C, Chen Z, Sang Z, Lu K, Xu K, Wu H and Ju B-F 2023 A novel method for measuring radial and axial errors in a cylindrical coordinate system using a combined double ball bar *Meas. Sci. Technol.* **34** 055019
[8] Srinivasa N and Ziegert J C 1996 Automated measurement and compensation of thermally induced error maps in machine tools *Precis. Eng.* **19** 112–32
[9] Wang W, Yue S, Yang H, Xu K, Sun T, Lu K, Chen Z, Wang C, Cui X and Ju B 2024 Fast detection of geometric errors for three-axis machine tools with combined double-ball bars based on spatial circle detection *Meas. Sci. Technol.* **35** 035003
[10] Kim H-S 2005 Kinematic calibration of a Cartesian parallel manipulator *Int. J. Control. Autom. Syst.* **3** 453–60
[11] Slamani M, Nubiola A and Bonev I A 2012 Effect of servo systems on the contouring errors in industrial robots *Trans. Can. Soc. Mech. Eng.* **36** 83–96
[12] ISO 230 4 2005 Test code for machine tools-part 4: circular tests for numerically controlled machine tools *Part 4: Circular tests for numerically controlled machine tools*
[13] Fesperman R R, Moylan S P, Vogl G W and Donmez M A 2015 Reconfigurable data driven virtual machine tool: geometric error modeling and evaluation *CIRP Ann.-Manuf. Sci. Technol.* **10** 120–30
[14] Andolfatto L, Lavernhe S and Mayer J R R 2011 Evaluation of servo, geometric and dynamic error sources on five-axis high-speed machine tool *Int. J. Mach. Tool Manuf.* **51** 787–96
[15] Engineers Aso M 1993 *Methods for Performance Evaluation of Computer Numerically Controlled Machining Centers* (American Society of Mechanical Engineers)
[16] Liu C, Xiang S, Lu C, Wu C, Du Z and Yang J 2020 Dynamic and static error identification and separation method for three-axis CNC machine tools based on feature workpiece cutting *Int. J. Adv. Manuf. Technol.* **107** 2227–38
[17] Elvira-Ortiz D A, Romero-Troncoso R D J, Jaen-Cuellar A Y, Morales-Velazquez L and Osornio-Rios R A 2016 Vibration suppression for improving the estimation of kinematic parameters on industrial robots *Shock Vib.* **2016** 6954012
[18] Brecher C, Brozio M, Klatte M, Lee T H and Tzanetos F 2017 Application of an unscented Kalman filter for modeling multiple types of machine tool errors *Proc. CIRP* **63** 449–54
[19] Eberhart R and Kennedy J, ed 1995 A new optimizer using particle swarm theory *MHS'95 Proc. 6th Int. Symp. on Micro Machine and Human Science* (*4–6 October 1995*)
[20] Kennedy J and Eberhart R, ed 1995 Particle swarm optimization *Proc. ICNN'95—Int. Conf. on Neural Networks* (*27 November–1 December 1995*)
[21] Kulkarni M N K, Patekar M S, Bhoskar M T, Kulkarni M O, Kakandikar G M and Nandedkar V M 2015 Particle swarm optimization applications to mechanical engineering- a review *Mater. Today* **2** 2631–9
[22] Zhang Y, Wang S and Ji G 2015 A comprehensive survey on particle swarm optimization algorithm and its applications *Math. Probl. Eng.* **2015** 931256
[23] Lai X, Qin C, Gao W, Zheng Y and Yi W 2018 A state of charge estimator based extended Kalman filter using an electrochemistry-based equivalent circuit model for lithium-ion batteries *Appl. Sci.* **8** 1592
[24] Jatoth R K, Rao D N and Kumar K S ed 2010 Particle swarm optimization aided unscented Kalman filter for ballistic target tracking *2010 Int. Conf. on Communication Control and Computing Technologies*
[25] Slamani M, Nubiola A and Bonev I 2012 Assessment of the positioning performance of an industrial robot *Ind. Robot.* **39** 57–68
[26] Kakino Y, Ihara Y, Shinohara A, Heidenhain J and Knapp W 1993 *Accuracy Inspection of NC Machine Tools by Double Ball Bar Method* (Hanser)
[27] Urrea C and Agramonte R 2021 Kalman filter: historical overview and review of its use in robotics 60 years after its creation *J. Sens.* **2021** 9674015
[28] Merwe R V D and Wan E, ed 2001 The square-root unscented Kalman filter for state and parameter-estimation. *2001 IEEE Int. Conf. on Acoustics, Speech, and Signal Processing. Proc. (Cat. No.01CH37221)* (*7–11 May 2001*)
[29] Wang L and Ding R 2020 A parameter determination method of unscented transformation and its approximate ability analysis in the precision estimation of nonlinear measurement adjustment *Measurement* **166** 108065
[30] Wan E and Merwe R V D, ed 2000 The unscented Kalman filter for nonlinear estimation *Proc. IEEE 2000 Adaptive Systems for Signal Processing, Communications, and Control Symp. (Cat. No.00EX373)* (*4–4 October 2000*)
[31] Julier S J, ed The scaled unscented transformation. *Proc. 2002 American Control Conf. 2002* (*8–10 May 2002*)
[32] Chatzis M N and Chatzi E N 2017 A discontinuous unscented Kalman filter for non-smooth dynamic problems *Front. Built Environ.* **3** 56
[33] Tao Y, Both A, Silveira R I, Buchin K, Sijben S, Purves R S, Laube P, Peng D, Toohey K and Duckham M 2021 A comparative analysis of trajectory similarity measures *GISci. Remote Sens.* **58** 643–69
[34] Bellman R and Kalaba R 1959 On adaptive control processes *IRE Trans. Autom. Control* **4** 1–9
[35] Alt H, Knauer C and Wenk C 2004 Comparison of distance measures for planar curves *Algorithmica* **38** 45–58
[36] Kate R J 2016 Using dynamic time warping distances as features for improved time series classification *Data Min Knowl. Discov.* **30** 283–312
[37] Lyu D, Liu Q, Liu H and Zhao W 2020 Dynamic error of CNC machine tools: a state-of-the-art review *Int. J. Adv. Manuf. Technol.* **106** 1869–91
[38] Kato N, Tsutsumi M and Sato R 2013 Analysis of circular trajectory equivalent to cone-frustum milling in five-axis machining centers using motion simulator *Int. J. Mach. Tool Manuf.* **64** 1–11
[39] Zhou R, Kauschinger B and Ihlenfeldt S 2021 Data synchronization by continuous spatial measurement with Double Ballbar *Measurement* **174** 108909
[40] Renishaw 2009 Renishaw QC20-W ballbar system help (available at: www.renishaw.com/resourcecentre/download?data=124307&lang=en&userLanguage=en)
[41] Císar M, Tlach V and Zajačko I 2022 Various methods of circular interpolation performance analysis *MATEC Web Conf.* **357** 01004